Available online at www.sciencedirect.com
ScienceDirect
Cement and Concrete Research 37 (2007) 455–468
Cement and Concrete Research

Modeling the effect of temperature on ionic transport in cementitious materials

E. Samson [a,*], J. Marchand [a,b]

[a] CRIB-Département de génie civil, Université Laval, Ste-Foy (Qc), Canada G1K 7P4
[b] SIMCO Technologies inc., 1400, boul. du Parc Technologique, Québec (Qc), Canada G1P 4R7

Received 7 September 2006; accepted 2 November 2006

Abstract

This paper deals with the effect of temperature on ionic transport in cementitious materials. The necessary steps to modify a model designed to work in isothermal conditions to take temperature variations of the environment into account are described. The following parts of the model were modified: transport properties, ionic transport and chemical reactions. Simulations of laboratory tests and field concrete measurements are presented.

Keywords: Ionic diffusion; Temperature; Chemical reactions; Diffusion coefficients; Chloride transport; Soret effect

1. Introduction

The basic principles of the influence of temperature on degradation kinetics on ionic transport are easy to understand. At low temperature, ionic diffusion and chemical reactions are slowed down. On the contrary, structures exposed to hot climates will potentially deteriorate more rapidly due to increased transport and chemical reaction rates. Making simulations with parameters evaluated at room temperature can thus result in underestimating or overestimating the service-life of a structure, depending on its environment. Despite the important role of temperature on ionic transport in cementitious materials, it is most of the time overlooked.

This paper presents the different steps that were performed to develop an ionic transport model that takes into account the effect of temperature. The starting point of the development is the isothermal model called STADIUM® presented in [1,2]. This multiionic transport model sequentially solves the mass conservation equations associated to each ionic species and the chemical equilibrium relationships for the chemical reactions between the pore solution and the hydrated cement paste (see [3] for a description of the sequential approach). The mass conservation equation for each ionic species considers the electrical coupling between the ionic species to enforce electroneutrality in the pore solution, the chemical activity, and advection due to water content gradients:

$$\frac{\partial(wc_i)}{\partial t} - \mathrm{div}\left(D_i w\ \mathrm{grad}(c_i) + \frac{D_i z_i F}{RT} wc_i\ \mathrm{grad}(\psi) + D_i wc_i\ \mathrm{grad}(\ln\gamma_i) + c_i D_w\ \mathrm{grad}(w)\right) = 0 \quad (1)$$

where c_i is the concentration of species i in the pore solution [mmol/L], w is the water content [m^3/m^3], D_i is the diffusion coefficient [m^2/s], z_i is the valence number, F is the Faraday constant [96,488.46 C/mol], ψ is the electrodiffusion potential [V], R is the ideal gas constant [8.3143 J/mol/°K], T is the temperature [°K], γ_i is the activity coefficient, and D_w is the

* Corresponding author.
E-mail address: esamson@simcotechnologies.com (E. Samson).

0008-8846/$ - see front matter © 2006 Elsevier Ltd. All rights reserved.
doi:10.1016/j.cemconres.2006.11.008

water diffusivity [m^2/s]. The chemical activity coefficients are calculated using the modified Davies model [4]. More details on this activity model are given in Section 4.

The diffusion coefficient is expressed as:

$$D_i = \underbrace{\tau\, D_i^o}_{\text{saturated}} \underbrace{\left(\frac{w^{7/3}}{\phi_o^{7/3}}\right)}_{\text{unsaturated effect}} \underbrace{\left(\frac{\phi}{\phi_o}\right)^3 \left(\frac{1-\phi_o}{1-\phi}\right)^2}_{\text{chemical effect}} \tag{2}$$

where τ is the tortuosity of the material [–], D_i^o [m^2/s] is the diffusion coefficient of species i in freewater, ϕ is the porosity [m^3/m^3], and ϕ_o is the initial porosity of the material. The first part of the expression gives the diffusion coefficient of the ionic species for saturated materials. The second term accounts for the reduction of the diffusion coefficient for unsaturated materials. It is based on the relationship derived by Millington and Quirk [5]. Finally, the last term accounts for local variations of porosity due to solid phases being dissolved or precipitated following chemical reactions. The correction is based on the Kozeny–Carman model [6]. The variation in porosity is calculated from the solid phases estimated at the previous time step.

To solve for the electrochemical potential ψ, the mass conservation equations are coupled to Poisson's relationship:

$$\text{div}\,(\tau w\ \text{grad}\,\psi) + \frac{F}{\varepsilon} w \left(\sum_{i=1}^{N} z_i c_i\right) = 0 \tag{3}$$

where ε [C/V/m] is the medium permittivity and N is the number of ions in the pore solution. Eq. (1) is also coupled to Richards' model, which allows calculating the water content field based on a diffusion approach:

$$\frac{\partial w}{\partial t} - \text{div}(D_w\ \text{grad}(w)) = 0 \tag{4}$$

The system of Eqs. (1)–(4) is solved using the finite element method. The simulations presented later in the paper are all concerned with 1D ionic transport cases. The ionic species considered in the calculations are: OH^-, Na^+, K^+, SO_4^{2-}, Ca^{2+}, $Al(OH)_4^-$ and Cl^-.

After the transport step, the concentrations at each node of the mesh are analyzed with a separate chemical equilibrium module that solves the following dissolution/precipitation relationship for the solid phases [7]:

$$K_m = \prod_{i=1}^{N} c_i^{\nu_{mi}} \gamma_j^{\nu_{mi}} \qquad \text{with} \quad m = 1, \ldots, M \tag{5}$$

where M is the number of solid phases, N is the number of ions, K_m is the equilibrium constant (or solubility constant) of the solid m, c_i is the concentration of the ionic species i, γ_i is its chemical activity coefficient, and ν_{mi} is the stoichiometric coefficient of the ith ionic species in the mth mineral. Upon dissolution and precipitation, the concentrations in the pore solution as well as the solid contents in the hydrated cement paste are adjusted to respect equilibrium. Table 1 lists the mineral phases considered in the model.

The formation of Friedel's salt due to chloride ingress in the material is based upon an ion-exchange mechanism [8]:

$$\underbrace{[AF_m^+ - SO_4^{2-}]}_{\text{monosulfates}} + 2Cl^- \rightleftharpoons \underbrace{[AF_m^+ - 2Cl^-]}_{\text{Friedel's salt}} + SO_4^{2-} \tag{6}$$

Following ionic-exchange theory [9], the equilibrium relationship for this reaction is expressed as:

$$K_{Cl/SO_4} = \frac{\{Cl\}^2}{\{SO_4\}} \frac{[AFm_{SO4}]}{[AFm_{Cl}]} \tag{7}$$

where the curly braces indicate activity [mmol/L], calculated according to the modified Davies model, and the square brackets correspond to the solid content per mass of material [mmol/g]. The equilibrium constant value is given in Table 1.

This isothermal model was modified in three separate steps:

- modeling the temperature field in concrete,
- evaluating the effect of temperature on the diffusion coefficients in cementitious materials,
- modeling the effect of temperature on chemical reactions.

These items are described in the following sections. In the last sections, simulation results are presented and compared to chloride profile measurements.

Table 1
Solid phases considered in the simulations

Reaction	−log(Ksp)
Minerals	
Portlandite	5.2
C–S–H	6.2
Ettringite	44.0
Monosulfate	29.4
Ion-exchange	
Monosulfate → Friedel's salt	−3.0

It is assumed that only a fraction of the total C–S–H can dissolve, according to the approach from [10]. This fraction is modeled like portlandite with a lower equilibrium value.

2. Modeling the temperature field

2.1. Energy balance equation

Different modeling approaches have been proposed to predict temperature in porous materials. The most comprehensive consists of resolving the energy balance equation for each phase in the porous medium. This approach was used by Schrefler [11] to model the temperature and humidity fields in concrete structures exposed to fire. The equations are coupled through balance equations at the interfaces between each phase. However, these terms prove difficult to evaluate and are most of the time neglected.

The most commonly used approach consists of considering a single mass conservation equation with average material parameters to account for the different phases. In [12,13],

energy conservation is modeled using the general conservation equation:

$$\frac{\partial M}{\partial t} + \mathrm{div}(F) = q \tag{8}$$

where M [J/m^3] is the energy accumulation term:

$$M = \phi(s_l\rho_l U_l + s_g\rho_g U_g) + (1-\phi)\rho_s U_s \tag{9}$$

where ϕ is the porosity [m^3/m^3], s is the saturation level [m^3/m^3], and U is the specific internal energy [J/kg]. The subscripts l, g, and s stand for the liquid, gaseous and solid phases. The flow term F [J/m^2/s] in Eq. (8) is given by:

$$F = h_l\rho_l v_l + h_g\rho_g v_g - \kappa\ \mathrm{grad}(T) \tag{10}$$

where h is the specific enthalpy [J/kg], v is the phase velocity and κ [W/m^2/°K] is the effective material heat conductivity. The term q [J/m^3/s] in Eq. (8) is a general source/sink term.

A similar model is proposed in [14,15]. To further simplify the approach, the energy accumulation term summing the contribution of all phases is lumped into a single average heat capacity parameter. The authors consider various source/heat terms q_n to account for phase changes due to drying and the hydration of cement:

$$\rho C_p \frac{\partial T}{\partial t} - \mathrm{div}\left(\kappa\ \mathrm{grad}(T) - C_{pl}\rho_l v_l T - C_{pg}\rho_g v_g T\right) = \sum q_n \tag{11}$$

where C_p [J/kg/°C] is the effective specific heat of the porous material.

In most situations, the energy associated with water vaporization as well as the heat transported by the gas flow v_g contribute only slightly to the overall temperature field. In these cases, the temperature field in porous materials can be modeled as [7]:

$$\rho C_p \frac{\partial T}{\partial t} - \mathrm{div}\left(\kappa\ \mathrm{grad}(T) - C_{pl}\rho_l v_l T\right) = 0 \tag{12}$$

Cement hydration has an important influence on temperature only during the first few hours after the material is put in place. Accordingly, for the prediction of the long-term behavior of the material, it can be neglected. Similarly, liquid phase flows in cementitious material are generally weak. The advection term $C_{pl}\rho_l v_l T$ in Eq. (12) becomes negligible. This leaves the following energy balance equation:

$$\rho C_p \frac{\partial T}{\partial t} - \mathrm{div}(\kappa\ \mathrm{grad}(T)) = 0 \tag{13}$$

This last equation is used to model temperature in the present paper. It is assumed that the density ρ and the effective specific heat C_p are constant parameters. The effective heat conductivity κ is expressed as:

$$\kappa = \kappa^{\mathrm{ref}}(0.244(S-1)+1)\ (0.0015(T-T^{\mathrm{ref}})+1) \tag{14}$$

where κ^{ref} correspond to the conductivity measured at the laboratory temperature T^{ref}. The parameter S is the saturation, calculated as w/ϕ. This expression is determined from data published in [18]. For $T=T^{\mathrm{ref}}$ and $S=1$, $\kappa=\kappa^{\mathrm{ref}}$.

2.2. Modification to the solute conservation equation

The isothermal solute conservation relationship given in Eq. (1) is derived from the electrochemical potential expression:

$$\mu_i = \mu_i^o + RT\ln(\gamma_i c_i) + z_i F\psi \tag{15}$$

where μ_i is the electrochemical potential and μ_i^o is a reference value for μ_i. The ionic flux is given as [19]:

$$j_i = -\frac{D_i^o}{RT} c_i\ \mathrm{grad}(\mu_i) + c_i v \tag{16}$$

where D_i^o is the diffusion coefficient in free solution. The flux is calculated by substituting Eq. (15) in Eq. (16) and assuming a constant temperature. The flux expression is then averaged over a representative elementary volume to obtain Eq. (1).

Substituting Eq. (15) in Eq. (16) without the constant temperature assumption gives the following ionic flux expression:

$$j_i = -D_i^o\ \mathrm{grad}(c_i) - \frac{D_i^o z_i F}{RT} c_i\ \mathrm{grad}(\psi) + D_i^o c_i\ \mathrm{grad}(\ln\gamma_i) - \underbrace{\frac{D_i^o c_i \ln(\gamma_i c_i)}{T}\mathrm{grad}(T)}_{\text{temperature coupling}} + c_i v \tag{17}$$

The underbraced term couples the solute concentration to the thermal gradient. This thermodiffusion flux is called the Soret effect [20]. Upon integration over a representative elementary volume following the homogenization technique presented in [1], this flux equation leads to the modified solute conservation equation:

$$\frac{\partial(wc_i)}{\partial t} - \mathrm{div}\left(D_i w\ \mathrm{grad}(c_i) + \frac{D_i z_i F}{RT} wc_i\ \mathrm{grad}(\psi) + D_i wc_i\ \mathrm{grad}(\ln\gamma_i) + \frac{D_i c_i \ln(\gamma_i c_i)}{T}\mathrm{grad}(T) + c_i D_w \mathrm{grad}(w)\right) = 0 \tag{18}$$

This equation is coupled to Eqs. (3), (4) and (13) to solve the concentrations, diffusion potential, water content and temperature fields. Special care must be taken when solving this equation due to the $\ln(\gamma_i c_i)$ term that is singular when the concentrations are equal to zero. Evaluating the limit using the Hospital rule shows that the term tends to zero when concentrations tend to zero.

2.3. Phase change considerations

Eq. (13) does not take into account the effect of the ice formation/melting on the temperature profiles. When this phenomenon occurs, liquid water locally releases a large amount of energy before being changed into ice. This energy is called the latent heat L [J/kg]. This sudden release of energy at the phase change front is known to be difficult to model given

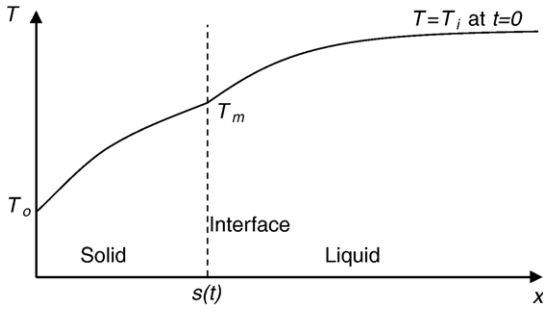

Fig. 1. The phase change problem.

its highly nonlinear nature. The objective of this subsection is to validate the assumption that ice formation does not have a strong influence on the temperature profile in cementitious material and can thus be neglected.

The demonstration is based on the analytical solution of the phase change problem, also known as the Stefan problem. It is presented in numerous heat transfer textbooks, such as [21]. It is assumed that initially, a liquid phase is at a temperature $T=T_i$ over the half-space $0\leq x<\infty$. At $t=0$, the temperature T_o is applied at the boundary $x=0$. The initial temperature T_i is higher than the phase change temperature T_m, and T_o is lower. As the temperature is lowered below T_m, a phase change front located at $x=s(t)$ will move from the external boundary to the interior of the material. The problem is summarized in Fig. 1. It is formulated as:

$$\rho_s C_{ps}\frac{\partial T_s}{\partial t}-\kappa_s\frac{\partial^2 T_s}{\partial x^2}=0 \qquad \text{in} \quad 0<x<s(t), t>0 \tag{19}$$

$$\rho_l C_{pl}\frac{\partial T_l}{\partial t}-\kappa_l\frac{\partial^2 T_l}{\partial x^2}=0 \qquad \text{in} \quad s(t)<x<\infty,\ t>0 \tag{20}$$

where the subscripts s and l correspond to the solid and liquid phases respectively. It is assumed that the thermal properties within each phase are constant. To consider the phase change, the following energy conservation equation at the interface is considered:

$$\kappa_s\frac{\partial T_s}{\partial x}-\kappa_l\frac{\partial T_l}{\partial x}=\rho_s L\frac{\mathrm{d}s(t)}{\mathrm{d}t} \qquad \text{at} \quad x=s(t),\ t>0 \tag{21}$$

which states that there is heat flux difference at the interface between the two phases and it corresponds to the energy released during the phase change. Finally, the temperature coupling condition is considered:

$$T_s(x,t)=T_l(x,t)=T_m \qquad \text{at} \quad x=s(t), t>0 \tag{22}$$

The solution over the half-space $0\leq x<\infty$ is given by the following set of equations:

$$\frac{e^{-\lambda^2}}{\mathrm{erf}(\lambda)}+\frac{\kappa_l}{\kappa_s}\sqrt{\frac{\alpha_s}{\alpha_l}}\left(\frac{T_m-T_o}{T_m-T_i}\right)\times\frac{e^{-\lambda^2(\alpha_s/\alpha_l)}}{\mathrm{erfc}(\lambda\sqrt{\alpha_s/\alpha_l})}-\frac{\lambda L\sqrt{\pi}}{\rho_s C_{ps}(T_m-T_o)}=0 \tag{23}$$

$$s(t)=2\lambda\sqrt{\alpha_s t} \tag{24}$$

$$T_s(x,t)=T_o+(T_m-T_o)\frac{\mathrm{erf}(x/\sqrt{4\alpha_s t})}{\mathrm{erf}(\lambda)} \qquad \text{for } x<s(t) \tag{25}$$

$$T_l(x,t)=T_i+(T_m-T_i)\frac{\mathrm{erfc}(x/\sqrt{4\alpha_l t})}{\mathrm{erfc}(\lambda\sqrt{\alpha_s/\alpha_l})} \qquad \text{for } x>s(t) \tag{26}$$

where $\alpha=\kappa/(\rho C_p)$ is the thermal diffusivity. The value of λ first has to be numerically determined from the transcendental Eq. (23). After that, the temperature profiles in the solid and liquid phase are determined according to Eqs. (25) and (26) respectively. The position of the phase change front is calculated according to Eq. (24).

Using this analytical solution, comparisons are made between temperature profiles for pure water and concrete. Both calculations are made with the latent heat of water being equal to 3.35×10^5 J/kg. The thermal properties for each case are given in Table 2. The data for pure water were taken from [22]. Temperature profiles are calculated after 24 h for the following initial and boundary conditions: $T_i=20$ °C and $T_o=-10$ °C. With these data, the value of λ that solves Eq. (23) is 0.28573. For concrete, the thermal conductivity above T_m is 1.5 W/s/°C [18]. Values of conductivities below the freezing temperature could not be found. Daoud et al. [23] published a study on the temperature prediction in dams exposed to freezing and thawing cycle using a constant conductivity. Based on this analysis, a constant conductivity is also used in this paper. The values for heat capacities above and below the freezing point were obtained from low-temperature calorimetry measurements performed on concretes made with CSA Type 10 cement and having water to cement ratios of 0.5 and 0.65. The results are shown in Fig. 2. Based on these measurements, the heat capacity above the freezing point is set at 1000 J/kg/°C. Below the freezing point, a value of 1200 J/kg/°C is used. The critical temperature T_m is set at −4 °C for the calculations. Using these parameters with $T_i=20$ °C, $T_o=-10$ °C, and $t=24$ h, the value

Table 2
Parameters used for the phase change calculations based on the analytical solution to Stefan problem

Materials	Properties	Values
Water	T_m [°C]	0.0
	Solid	
	Heat capacity [J/kg/°C]	2239.0
	Density [kg/m^3]	920.0
	Conductivity [W/m/°C]	2.3
	Liquid	
	Heat capacity [J/kg/°C]	4186.0
	Density [kg/m^3]	1000.0
	Conductivity [W/m/°C]	0.56
Concrete	T_m [°C]	−4.0
	Below T_m	
	Heat capacity [J/kg/°C]	1200.0
	Density [kg/m^3]	2400.0
	Conductivity [W/m/°C]	1.5
	Above T_m	
	Heat capacity [J/kg/°C]	1000.0
	Density [kg/m^3]	2400.0
	Conductivity [W/m/°C]	1.5

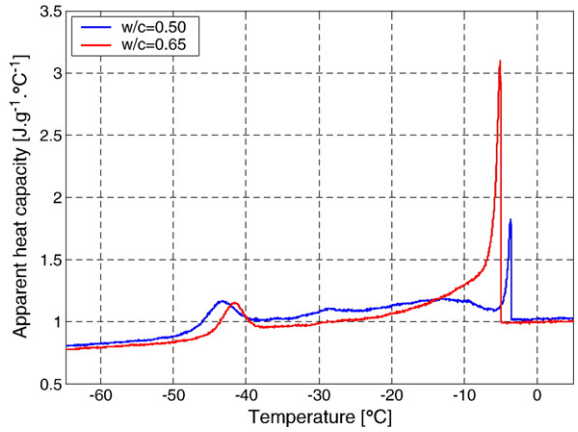

Fig. 2. Measured heat capacity on concrete samples.

of lambda that solves Eq. (23) is 0.19532. The results are shown in Fig. 3.

The results are compared with the analytical solution of the heat conduction equation when the phase change is neglected and the liquid phase properties are assumed for the whole temperature range. In that case, the profiles are calculated from Eq. (26) with $\lambda=0$. Fig. 3a shows the strong influence of the heat released at the phase change front $s(t)$ on the temperature profile for pure water. However, in the case of concrete

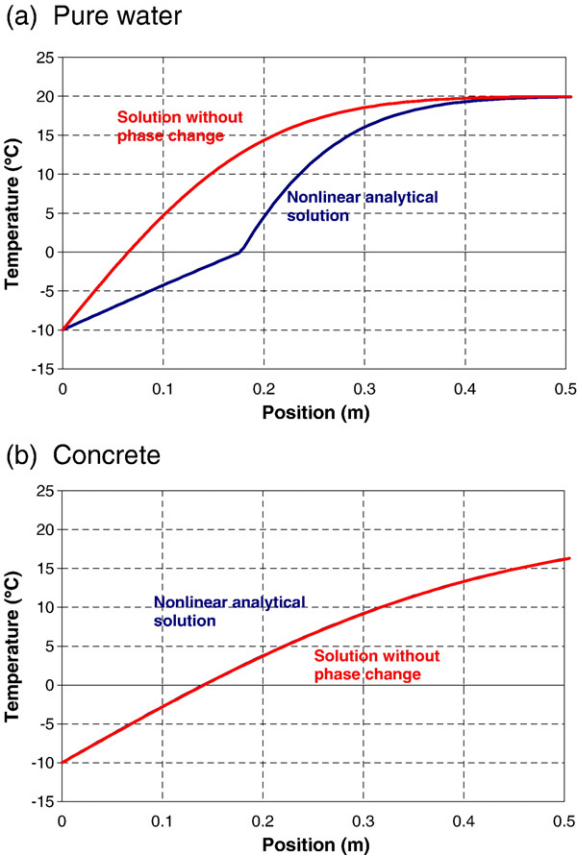

Fig. 3. Temperature profiles calculated from the analytical solution of the phase change problem for pure water and concrete.

Table 3
Summary of the experimental program

W/C	Hydration (days)	Migration tests performed					
		4 °C		23 °C		40 °C	
		Type 10	Type 50	Type 10	Type 50	Type 10	Type 50
0.45	28	x	x	x	x	x	x
	91	x	x	x	x	x	x
	365	x	x	x	x	x	x
0.65	28	x	x	x	x	x	x
	91	x	x	x	x	x	x
	365	x	x	x	x	x	x
0.75	28	x	x	x	x	x	x
	91	x	x	x	x	x	x
	365	x	x	x	x	x	x

(Fig. 3b), the presence of the large solid matrix volume contributes to dampen the effect of latent heat (concrete porosities are usually in the 9%–15% range). In that case, the contribution of the phase change energy on the temperature distribution is negligible. It should be noted that for very low temperatures (T ¡ −40 °C), the heat capacity drops below 1000 J/kg/°C. In that case, the difference in heat capacities for frozen and unfrozen material yields to temperature profiles that can be significantly affected by the phase change. However, this temperature range is not considered in most practical cases.

3. Effect of temperature on diffusion coefficients

3.1. Experiments

The experimental program consisted in performing migration tests on concrete samples in order to evaluate the diffusion coefficients of the ionic species. The tests were performed at 4 °C, 23 °C (reference value) and 40 °C. The concretes were prepared at three different water to cement ratios: 0.45, 0.65 and 0.75, with two different Canadian cements, Type 10 and 50. The migration tests were performed at 28, 91 and 365 days of hydration. The experimental program is summarized in Table 3. The mixture characteristics are given in Table 4. All mixtures were produced with a coarse aggregate made of crushed granite (5–14 mm) with a density of 2.67. The fine aggregate was a commercial granite concrete sand complying with CSA A23.2-2A. The density of the sand was 2.67. After the mixing sequence, cylindrical specimens (diameter: 10 cm, length: 20 cm) were cast. Demolding was done 24 h after casting. The specimens were then cured in a fog chamber (RH=100%, T=25 °C) for 28, 91 and 365 days respectively before testing.

Table 4
Concrete mixture characteristics

Materials	Mixture proportions (kg/m^3)		
	w/c=0.45	w/c=0.65	w/c=0.75
Cement (T10 and T50)	380	280	260
Water	171	182	195
Sand	719	833	915
Coarse aggregates	1127	1065	956

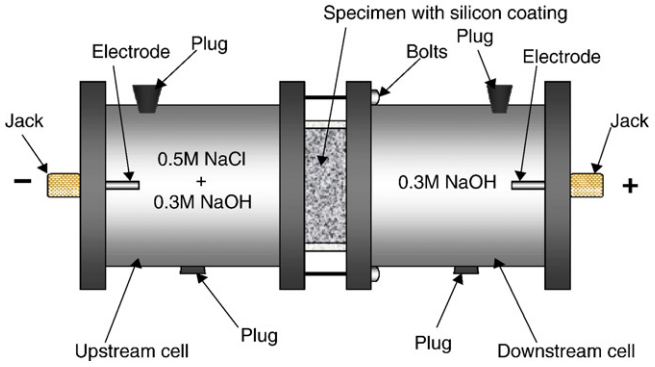

Fig. 4. Migration set-up.

The migration test is a modified version of the ASTM C1202 standard procedure. It consists of accelerating the transport of ions in a saturated concrete sample by applying an external electrical potential. The experimental set-up is shown in Fig. 4. To perform the test, two 50-mm thick discs were first cut from a saturated cylinder cured in a fog room. The lateral surface of the discs was coated with a silicon gel. The discs were then mounted on the migration cells. The cell/disc interface was also coated with silicon to ensure a watertight joint. Both compartments of the cells were filled with approximately 2.5 l of solution. The test solution on the upstream side of the cell was made of 300 mmol/L of sodium hydroxide (NaOH) and 500 mmol/L of sodium chloride (NaCl). The downstream compartment of the cell was filled with a 300 mmol/L sodium hydroxide solution. During the test, an external 20 V potential was applied to the cell, and the current passing through the samples was regularly measured over a 200-hour period.

Current values are then analyzed following the procedure described in Samson et al. [24] in order to evaluate the diffusion coefficients. The analysis is based on the numerical resolution of the extended Nernst–Planck equation. This equation is used to calculate a numerical current that matches the measured ones by finding the proper tortuosity parameter (see Eq. (2)). The analysis requires knowledge of the porosity, which is measured according to the ASTM C642 procedure. It also necessitates considering the initial pore solution concentrations of the material. The solution is extracted from the material by applying a load on a crushed sample. Porosity and pore solution data were published in [25]. The chloride diffusion coefficients presented in Table 5 correspond to the average of two values.

As expected, the diffusion coefficient values tend to increase with temperature. The results also emphasize the effect of the type of cement on diffusion coefficients. The coefficients for the concrete made with the Type 50 cement are systematically higher than the coefficients from the Type 10. The ratio Type 50/Type 10 has an average value of 1.5. The results also give information on the effect of hydration. The diffusion coefficients at 1 year for the 0.45 w/c materials are all lower than at 28 days, indicating that D_i for these materials are affected by hydration. For the higher w/c ratios, this systematic drop is not observed, thus showing no clear effect of hydration. Instead, the values evaluated on these material at different hydration period are scattered within the experimental error, which is estimated at 15% from the results published in [24].

3.2. Analysis

To quantify the effect of temperature on diffusion coefficients, the results presented in Table 5 are fitted to the following relationship:

$$D_i = D_i^{\mathrm{ref}} \mathrm{e}^{\alpha(T-T^{\mathrm{ref}})} \tag{27}$$

where the subscript ref corresponds to a reference value. For convenience, the reference value corresponds to the measurements made at room temperature. The values of α thus calculated are presented in Table 6. Interestingly, the results show no particular trend associated with the type of cement, the curing duration or the water to cement ratio. This is somehow surprising since it is in opposition with previously published temperature vs. diffusion relationships. In [16,17], the effect of temperature on diffusion is modeled through the activation energy parameter and apparently exhibits a dependence on the water to cement ratio.

From these results, the parameter α is seemingly independent of the material. Calculating the value of α that best fits all the results in Table 6 gives: $\alpha = 0.028$. To confirm the assumption that α does not depend on the material, a similar analysis was performed using diffusion coefficient in freewater values found in textbooks [26] and measured at different temperatures.

Table 5
Chloride diffusion coefficients evaluated from the migration tests

W/C	Hydration (days)	Chloride diffusion coefficient (E−11 m^2/s)					
		4 °C		23 °C		40 °C	
		Type 10	Type 50	Type 10	Type 50	Type 10	Type 50
0.45	28	3.2	7.1	5.6	11.0	8.0	13.7
	91	3.0	4.5	5.2	7.5	6.7	11.3
	365	2.6	4.5	4.4	7.5	7.1	13.5
0.65	28	5.3	7.7	8.3	13.0	12.9	19.7
	91	5.3	7.3	8.0	11.4	14.5	19.7
	365	6.2	6.6	9.1	12.8	15.7	25.3
0.75	28	6.1	10.7	10.5	15.7	16.1	25.4
	91	6.7	9.4	11.5	15.0	18.8	23.1
	365	7.4	10.3	11.9	16.7	19.4	27.0

Table 6
Value of the parameter á calculated separately for each concrete mixture according to Eq. (27)

W/C	Hydration (days)	α (1)	
		Type 10	Type 50
0.45	28	0.0248	0.0173
	91	0.0207	0.0272
	365	0.0314	0.0377
0.65	28	0.0283	0.0277
	91	0.0372	0.0346
	365	0.0341	0.0446
0.75	28	0.0286	0.0299
	91	0.0320	0.0280
	365	0.0313	0.0309

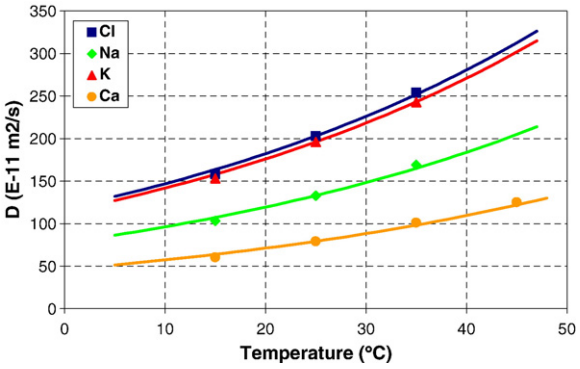

Fig. 5. Ionic diffusion coefficients in freewater as a function of temperature. The fitting was obtained with $\alpha = 0.022$.

Fitting the data with Eq. (27) (see Fig. 5) gives $\alpha = 0.022$, which is close to the value obtained for the concrete samples.

Finally, a similar analysis was performed for chloride diffusion coefficients measured for Vycor glass. The coefficients were obtained by performing a diffusion experiment on very thin (≈ 2 mm) sheet of Vycor glass exposed on one side to a 0.5 M NaCl solution and on the other side to pure water [27]. Chloride concentrations were measured in the downstream cell. The diffusion coefficients were evaluated using the steady-state chloride flux value fitted to Nernst–Planck equation. The experiment was performed at four different temperatures: 4 °C, 23 °C, 38 °C and 50 °C. The diffusion coefficient values are plotted in Fig. 6 as a function of temperature. Fitting the α parameter of Eq. (27) to these data gave a value of 0.024, again very close to the values obtained on concrete and freewater. This value was used to plot the fitting curve in Fig. 6.

The comparison with results obtained on other materials confirms that the effect of temperature on diffusion coefficients is indeed independent of the type of material. The discrepancy between the values estimated from freewater experiments ($\alpha = 0.022$) and migration tests ($\alpha = 0.028$) is attributed to the heterogeneity of concrete and to experimental errors. From the strict point of view of the diffusion mechanism, an increase in temperature only contributes to increase the thermal agitation of ions in solution without affecting the microstructure and consequently the tortuosity factor (see Eq. (2)) of the material.

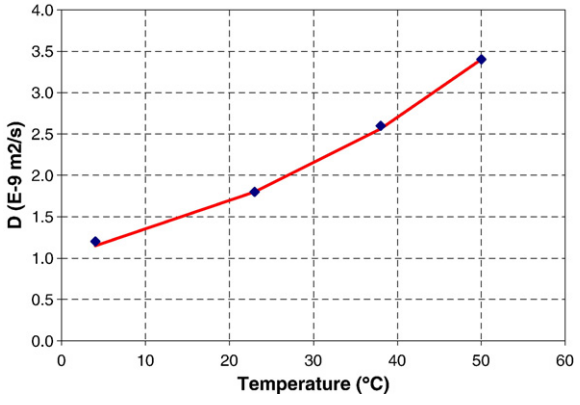

Fig. 6. Chloride diffusion coefficient estimated from a diffusion experiment on Vycor glass at different temperatures. The fitting was obtained with $\alpha = 0.024$.

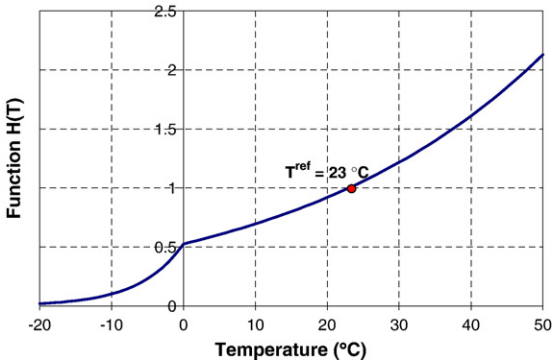

Fig. 7. Function $H(T)$ (Eq. (28)) with $T^{ref} = 23$ °C.

This assumption seems reasonable for the temperature range to which most structures are exposed. Even if the tortuosities are different from one material to the other, a similar temperature variation will affect the coefficients in the same proportions.

The evaluation of the effect of temperature on diffusion in the sub-freezing range poses some obvious technical difficulties. Furthermore, no data could be found in the literature on this topic. Before reliable technical data and experimental procedures are devised, assumptions to model ionic transport in this temperature range are needed. In this paper, it is assumed that the diffusion coefficient values drop rapidly below zero to reach a near-zero value at −20 °C. The proposed relationship $H(T)$ to account for the effect of temperature on diffusion is given by:

$$H(T) = \begin{cases} e^{0.028(T-T^{ref})} & \text{if } T \geq 0 \\ 1.18^{T} e^{-0.028T^{ref}} & \text{if } T < 0 \end{cases} \quad (28)$$

with T expressed in [°C]. This function multiplies the diffusion coefficient in Eq. (2). It is plotted in Fig. 7.

4. Effect of temperature on chemical reactions

In the equilibrium-based approach used to model chemistry (see Eq. (5)), temperature affects reactions by modifying the equilibrium constant value. The relationship between temperature and K_{sp} follows the Van't Hoff equation [28–30]:

$$\ln(K_{sp}) = \ln(K^{o}) + \frac{\Delta H^{o}}{R}\left(\frac{1}{T^{o}} - \frac{1}{T}\right) \quad (29)$$

where ΔH^{o} [J/mol] is the reaction enthalpy and the subscript o indicates reference values. The latter are usually measured at 25 °C. Table 7 gives values of ΔH^{o} for different mineral phases, as found in [28,31].

For C–S–H and Friedel's salt, data could not be found in the literature. In the present model, since it is assumed that the soluble part of C–S–H dissolves like portlandite, the same value of reaction enthalpy is used. This assumption could be verified by exposing paste samples to pure water at different temperatures and measuring the calcium profile with a microprobe (see [32]). This topic has not been addressed in the present paper.

Table 7
Reaction enthalpy for different minerals

Minerals	ΔH^o (kJ/mol)
Portlandite	−17.88
C–S–H [a]	−17.88
Monosulfate	45.57
Ettringite	204.5
Friedel's salt [a]	−150.0
Gypsum	−0.46
Calcite	−9.62
Brucite	−113.46
Mirabilite	79.5
Halite	3.84

[a] Estimated values — no data available.

For Friedel's salt, the value was estimated based on simulations of the experimental results presented in the next section. The first simulation at 4 °C was performed with $\Delta H^o = 0$, which means that the ion-exchange process driving chloride binding is not affected by temperature. The numerical results obtained showed that near the surface of the material exposed to the NaCl solution, the chloride profile at 4 °C enters the material more rapidly than at 23 °C, which does not correspond to the measurements presented in the next section. If the value of ΔH^o is increased, this anomalous ingress rate near the surface is also increased. However, for negative reaction enthalpy values, lowering the temperature tends to lower the chloride ingress rate, which corresponds to the experimental observations. A value of −150.0 kJ/mol allowed reproducing the chloride profiles measured at 4 °C. This value of reaction enthalpy for Friedel's salt also allows reproducing the chloride profile measured at 38 °C, as will be shown in the next section.

Due to the fact that the concrete pore solution is a concentrated electrolyte, all the chemical equilibrium calculations discussed previously require the evaluation of the ionic activity coefficients to yield reliable estimations, as emphasized in Eqs. (5) and (7). The activity coefficient calculations are performed with a modified version of the Davies equation [4]:

$$\ln\gamma_i = -\frac{Az_i^2\sqrt{I}}{1 + a_i B\sqrt{I}} + \frac{(0.2 - 4.17\times10^{-5} I)Az_i^2 I}{\sqrt{1000}} \quad (30)$$

where I [mmol/L] is the ionic strength of the solution:

$$I = \frac{1}{2}\sum_{i=1}^{N} z_i^2 c_i \quad (31)$$

In Eq. (30), A and B are temperature dependant parameters, given by:

$$A = \frac{\sqrt{2}F^2 e_o}{8\pi(\varepsilon RT)^{3/2}} \quad (32)$$

$$B = \sqrt{\frac{2F^2}{\varepsilon RT}} \quad (33)$$

where e_o [1.602×10^{-19} C] is the electrical charge of one electron. The parameter a_i [m] in Eq. (30) depends on the ionic species. The values are given in [4].

To confirm the validity of the modified Davies model over a wide range of temperatures, comparisons were made with experimental activity values [33,34] measured between 0 °C and 50 °C, as shown in Fig. 8. The experimental results emphasize the weak dependence of the activity coefficients with temperature. The modified Davies model correctly estimates the activity coefficients over the considered temperature range. In most cases, the values estimated with the model are lower than the measured ones. But the variation between the two data sets is smaller than 3%. For the highly concentrated NaCl solution, the modeled values tend to decrease with temperature, whereas the measured ones have the opposite behavior. However, the maximum error observed is around 6% at 50 °C, which is deemed acceptable for ionic transport modeling.

5. Numerical implementation

With the addition of the temperature variable, the ionic transport model consists of a set of 11 equations: 8 mass conservation Eq. (18) for the species, one Eq. (3) for the electrodiffusion potential, one mass conservation Eq. (4) for

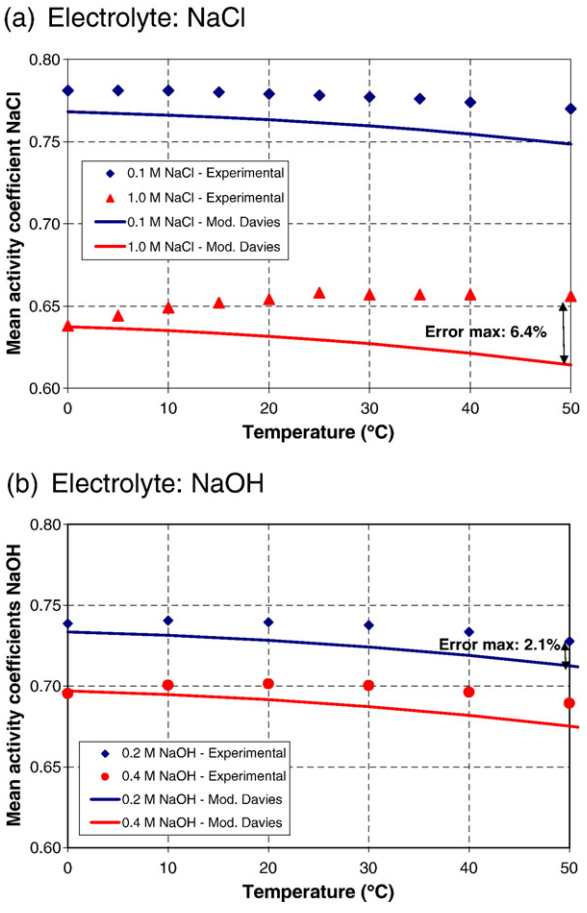

Fig. 8. Activity coefficients as a function of temperature calculated with the modified Davies model for different electrolytes.

liquid water, and finally one energy conservation Eq. (13) to account for temperature effect.

This set of equations is solved using the finite element method. The equations are solved simultaneously with a coupled approach. The space discretization is based on the Galerkin weighting. The time discretization relies on the implicit Euler scheme.

After the transport equations are solved, the model enters the chemical equilibrium module. The algebraic set of nonlinear Eqs. (5) and (7) that enforce the equilibrium between the pore solution and the solid phases of the hydrated cement paste is solved at each node of the finite element mesh using the Newton–Raphson algorithm. More details on the numerical implementation are given in [2].

6. Simulations

6.1. Laboratory validation

To validate the approach, immersion tests were performed on a neat cement paste cylinder exposed to a 0.5 M NaCl solution at 4, 23 and 38 °C. The immersions were performed on paste to obtain chloride profiles that are not affected by the aggregate content. The hydrated paste was prepared with an ordinary Canadian Type 10 portland cement at water to cement ratio of 0.6. The paste was prepared under vacuum to prevent the formation of air voids. Mixtures were cast in plastic cylinders (diameter=7.0 cm, height=20 cm). Molds were sealed and rotated for the first 24 h to prevent bleeding. After 3 months of curing in a 100% relative humidity fog room, 50-mm samples were cut and sealed on the bottom and side surface to enforce 1D ionic transport during the test. The samples immersed at 4 and 23 °C were sealed with wax whereas epoxy was used for the 38 °C exposure temperature. The samples were then immersed in a sodium chloride solution for 100 days in chambers kept at different temperatures. During immersion, the pH was measured on a regular basis. When its value reached 10.5, the solution was renewed, thus maintaining constant boundary conditions throughout the experiment. After the exposure period, the total chloride content in the sample was measured following the ASTM C1556 layer-by-layer acid dissolution procedure using 2–3 mm depth increments.

Table 8
Properties of the 0.6 w/c hydrated cement paste

Properties	Values	Properties	Values
Cement type	CSA, T10	Porosity	44.50%
w/c	0.6		
		Diffusion coefficients	(E−11 m^2/s)
Mixture proportions	(kg/m^3)	OH^-	18.50
Cement	1088.8	Na^+	4.7
Water	653.3	K^+	6.9
Coarse aggregates	–	SO_4^{2-}	3.7
Fine aggregates	–	Ca^{2+}	2.8
Density	1742.1	$Al(OH)_4^-$	1.9
		Cl^-	7.1
Cement composition	(% mass)		
CaO	61.7	Initial pore solution	(mmol/L)
SiO_2	19.1	OH^-	325.0
Al_2O_3	5.18	Na^+	98.6
SO_3	3.51	K^+	230.8
		SO_4^{2-}	3.3
Initial solid phases	(g/kg)	Ca^{2+}	1.2
Portlandite	195.5	$Al(OH)_4^-$	0.2
C–S–H	362.3	Cl^-	0.0
Ettringite	28.4		
Monosulfate	128.3	Conductivity (W/m/°C)	1.2
		Heat capacity (J/kg/°C)	1800

After the curing period, paste samples from the same batch were also analyzed to evaluate the transport properties of the material at 23 °C. The porosity was measured using the ASTM C642 procedure. Migration tests were performed on the 25-mm disks following the procedure described in [24] and in Section 3.1 to evaluate the diffusion coefficients. Finally, the initial pore solution was extracted from the sample by pore pressing. The parameters measured with these tests are summarized in Table 8. The pore solution presented in the table has been slightly corrected to respect the electroneutrality requirement and the chemical equilibrium of the solid phases.

The table also includes the initial amount of each solid phase in the material: portlandite (CH), C–S–H, ettringite (AFt) and monosulfates (AFm). It is calculated from the cement composition (CaO, SiO_2, Al_2O_3 and SO_3) by solving the following set of equations:

$$\frac{\Gamma_{Si}}{\Gamma_{csh}} S_{csh} = 10 SiO_2 \frac{\Gamma_{Ca}}{\Gamma_{SiO_2}} \tag{34}$$

$$3\frac{\Gamma_s}{\Gamma_{AFt}} S_{AFt} + \frac{\Gamma_s}{\Gamma_{AFm}} S_{AFm} = 10\ SO_3 \frac{\Gamma_s}{\Gamma_{SO_3}} \tag{35}$$

$$2\frac{\Gamma_{Al}}{\Gamma_{AFt}} S_{AFt} + 2\frac{\Gamma_{Al}}{\Gamma_{AFm}} S_{AFm} + 2\xi_{Al_2O_3} \frac{\Gamma_{Al}}{\Gamma_{Al_2O_3}} S_{csh} = 10\ Al_2O_3 \frac{2\Gamma_{Al}}{\Gamma_{Al_2O_3}} \tag{36}$$

$$\frac{\Gamma_{Ca}}{\Gamma_{CH}} S_{CH} + 1.65\frac{\Gamma_{Ca}}{\Gamma_{csh}} S_{csh} + 6\frac{\Gamma_{Ca}}{\Gamma_{AFt}} S_{AFt} + 4\frac{\Gamma_{Ca}}{\Gamma_{AFm}} S_{AFm} = 10\ CaO \frac{\Gamma_{Ca}}{\Gamma_{CaO}} \tag{37}$$

where the Γ_is are the different molar masses. The factor 10 on the right-hand side of each equation is used to change the mass of the cement components from % to [g/kg]. The term ξ_{Al_2O3} is an amount of Al_2O_3 that substitutes in the C–S–H. According to [35], that substitution rate varies between 2% and 5%. The value of 2.5% is used for the calculations. To account for the degree of hydration of the material, the quantity of CaO, SiO_2, Al_2O_3 and SO_3 should be multiplied by the appropriate factor, i.e. multiply each quantity by 0.9 for a 90% hydration degree. Given the high w/c ratio of the mixture and the three-month cure in a fog room, it was assumed that the material was fully hydrated.

The thermal conductivity was estimated from experimental measurements found in [18]. The heat capacity was derived from low temperature calorimetry measurements performed on paste samples made with a CSA Type 10 cement at 0.5 and 0.75

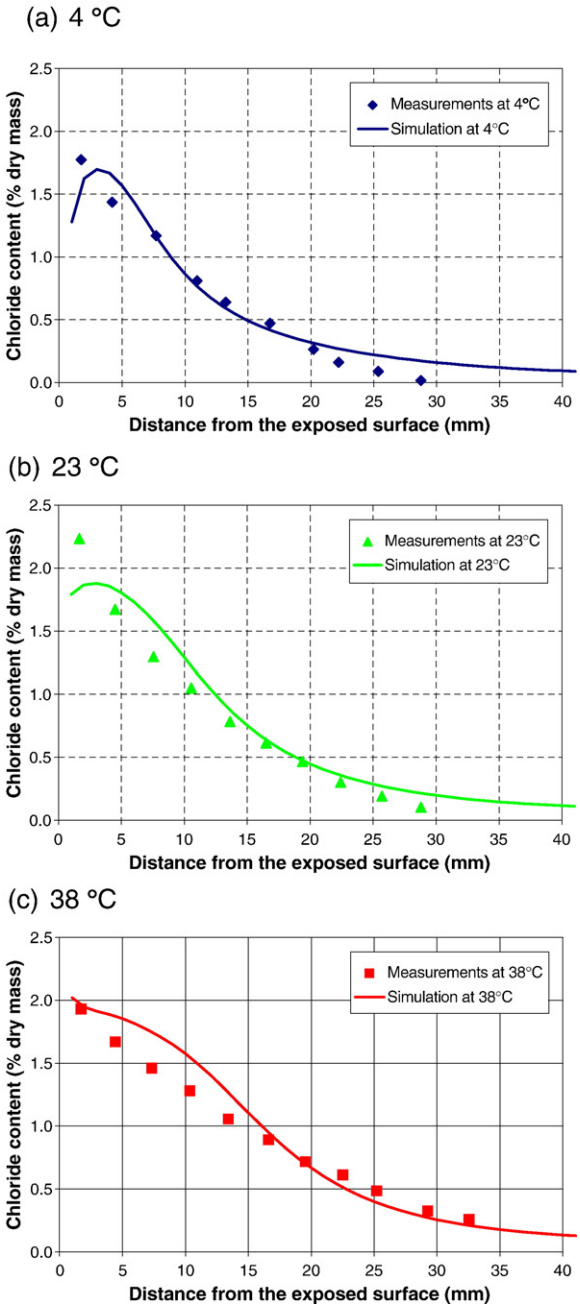

Fig. 9. Comparison of the numerical simulations with the chloride profiles measured after 100 days of exposure at three different temperatures.

water to cement ratios. The interpolation between the two sets of results gives 1800 J/kg/°C. Simulations showed that the temperature in the paste samples only takes a few hours to be in equilibrium with the surrounding immersion solution. The calculations are thus not very sensitive to the thermal properties, the transient thermal period being very short compared to the overall experiment duration. The thermal properties are reported in Table 8.

The boundary conditions for the chemical environment consist in imposed values on the first node of the mesh. The imposed concentrations are 500 mmol/L for Na^+ and Cl^-. The concentrations are gradually increased to reach 500 mmol/L after 2 days to avoid numerical oscillations. For all the other species, a zero value is imposed at the same node at $t=0$. For the water content variable, a value corresponding to the porosity is imposed at $x=0$ since the tests are performed in saturated conditions. A convection flux boundary condition is used for temperature: $q_n=h_T(T-T_\infty)$, with an exchange coefficient $h_T=8$ m/s. The values for T_∞ correspond to the immersion temperatures. Finally, the diffusion potential ψ is set to zero at $x=0$.

The numerical simulations are performed with a regularly spaced 50 element mesh over 50 mm. A 21,600 s (¼ day) time step is used. The total chloride content is calculated at the end of a simulation as the sum of chlorides in solution and chlorides bound as Friedel's salt. Both contributions are weighted appropriately to obtain a chloride content expressed in g per kg of dry material (‰).

The experimental results are shown in Fig. 9, along with the numerical simulations. There is a good correlation between the two sets of data. The model correctly takes into account the effect of temperature on the ionic transport process. Simulations considering separately the effect of temperature on diffusion and chemistry were also performed. The results of these calculations showed that the overall profile is influenced almost equally by both factors. At 4 °C for instance, neglecting the effect of temperature on chemistry yields a profile that is halfway between the numerical profiles at 4 °C and 23 °C in Fig. 9.

6.2. Parking structure simulation

The model was used in this section to simulate chloride ingress in an actual parking structure exposed in the winter to deicing salts. The parking is located in Quebec City (Canada). Cores were extracted from a 20-cm slab after 20 years of exposure. The model was used to reproduce the chloride profile measured for the concrete. This case is used not so much to further validate the model but rather to illustrate its application for the treatment of an actual structure.

Given the age of the structure, little information on the mixture was available. Records suggest that the concrete had a water to cement ratio of 0.45 with a compressive strength in the 35–40 MPa range at 28 days. It was also assumed that the concrete was prepared with an ordinary CSA Type 10 portland cement and that no supplementary cementitious materials had been used.

The transport properties were obtained from laboratory tests performed on a 0.45 concrete made with a CSA Type 10 portland cement cured for 28 days in a fog room. The material complied with the compressive strength range mentioned previously (40.4 MPa at 28 days). The mixture proportions and cement composition are summarized in Table 9. The procedures to obtain the porosity, pore solution, diffusion coefficients and solid phases have already been outlined in Section 3.1. The solid phases were calculated assuming a 90% degree of hydration for the cement and with $\xi_{Al_2O3}=2.5\%$. The results from those tests are given in Table 9 along with the chemical composition of the cement and the mixture proportions. The thermal properties were again taken from results found in [18].

Table 9
Properties of the concrete for the parking structure simulation

Properties	Values	Properties	Values
Cement type	CSA, T10	Diffusion coefficients	(e−11 m^2/s)
w/c	0.45	OH^-	10.1
		Na^+	2.6
Mixture proportions	(kg/m^3)	K^+	3.8
Cement	380	SO_4^{2-}	2.0
Water	171	Ca^{2+}	1.5
Coarse aggregates	1127	$Al(OH)_4^-$	1.0
Fine aggregates	719	Cl^-	3.9
Density	2397		
		Water diffusivity	
Cement composition	(% mass)	A (E−12 m^2/s)	1.4
CaO	62.1	B (–)	34.5
SiO_2	20.4		
Al_2O_3	4.3	Hydration parameters	
SO_3	3.2	a (–)	0.72
		α (1/s)	3.8E−03
Initial solid phases	(g/kg)		
Portlandite	45.1	Initial pore solution	(mmol/L)
C–S–H	88.3	OH^-	373.9
Ettringite	11.6	Na^+	178.3
Monosulfate	18.2	K^+	220.0
		SO_4^{2-}	13.5
Conductivity (W/m/°C)	2.2	Ca^{2+}	1.4
Heat capacity (J/kg/°C)	1000.0	$Al(OH)_4^-$	0.2
		Cl^-	0.0
Porosity	12.2%		

To account for the long-term effect of hydration on the transport properties, the data collected over several curing periods on a similar material (see the results for the 0.45 T10 at 23 °C in Table 5) were fitted to the following function:

$$h(t) = \frac{D_i(t)}{D_i(t^{\text{ref}})} = \frac{a}{1 + (a-1)e^{-\alpha(t-t^{\text{ref}})}} \quad (38)$$

This function has the following properties. When $t \to \infty$, $h(t) = a$. The parameter a [–] thus represents the fraction that multiplies the diffusion coefficients when the hydration process is completed. When $t = t^{\text{ref}}$, $h(t) = 1$. The reference time t^{ref} corresponds to a curing period of 28 days. The parameter α [1/s] characterizes the decreasing rate of the function. When diffusion coefficients are evaluated at different curing periods, it is possible

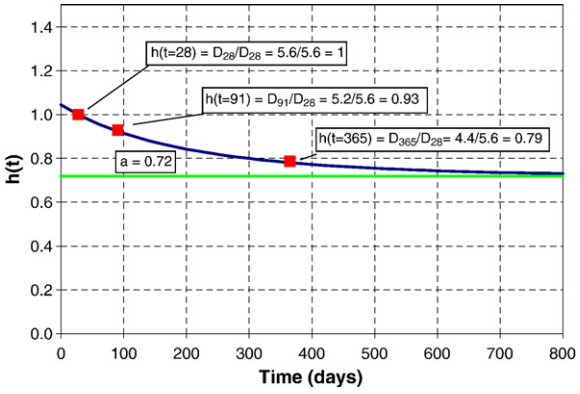

Fig. 10. Hydration function $h(t)$ (Eq. (38)) estimated from diffusion coefficient measurements.

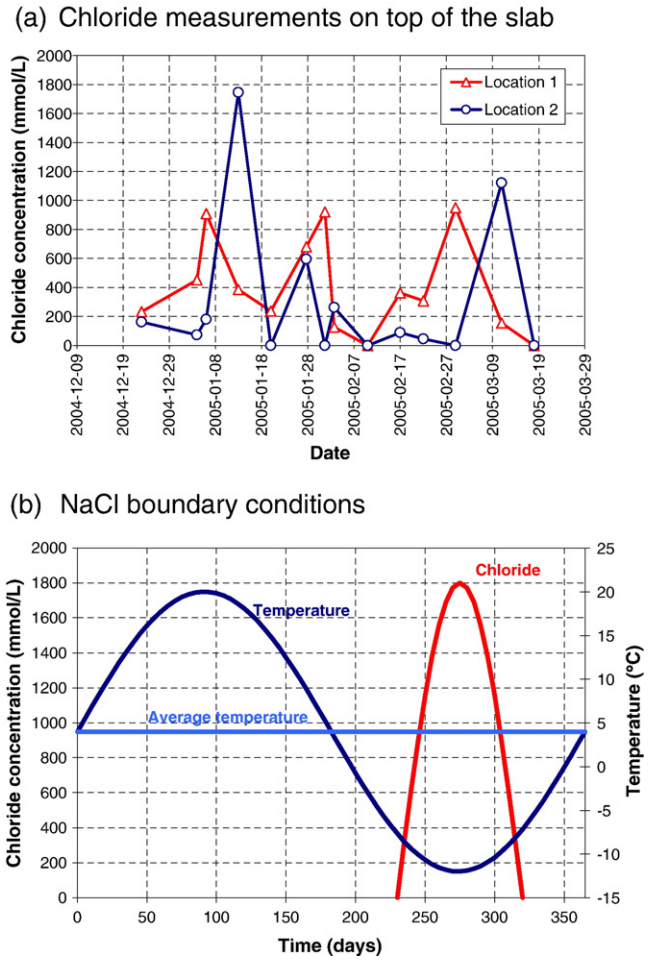

Fig. 11. Boundary conditions for the applied sodium chloride during 1 year.

to evaluate a and α. Based on the results at 23 °C for the 0.45 T10 material given in Table 5, the parameters a and α are 0.72 and 3.8×10^{-3} respectively. The function $h(t)$ is plotted in Fig. 10. It multiplies the diffusion coefficient given by Eq. (2).

Water transport properties are needed to perform the simulation since the structure does not remain saturated during its service-life. The water diffusivity parameter D_w was evaluated from a drying experiment performed on the same 0.45 w/c concrete made with CSA Type 10 cement used for the migration tests presented earlier in the paper. The material had been cured for 28 days in a fog room prior to the test. The test consists of exposing a disk of initially saturated material to two different relative humidities. In this case, the relative humidities were controlled by saturated NaCl (75% RH) and $MgNO_3$ (52% RH) salt solutions in tightly closed plastic boxes. The samples were sealed on one end and on the side to enforce 1D water transport. The mass of the samples was measured over approximately 1 month. Expressing the water diffusivity as an exponential function $D_w = Ae^{Bw}$ [36], Richards' Eq. (3) was used to reproduce the two mass loss curves by adjusting A and B. The analysis gave $A = 1.4 \times 10^{-12}$ m^2/s and $B = 34.5$. The values are reported in Table 9. It was assumed that the parameter D_w follows the same hydration effect $h(t)$ as the ionic species (Eq. (38)). Likewise, it was assumed in the model that D_w is

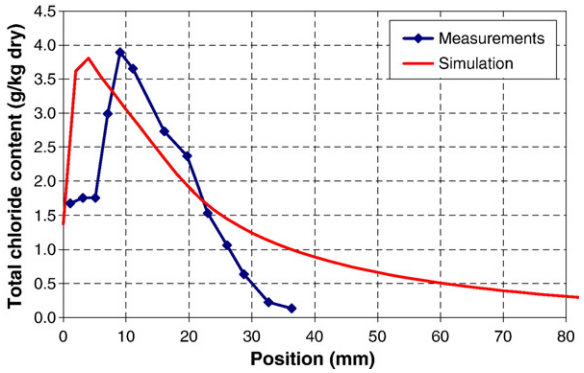

Fig. 12. Comparison between the measured and simulated chloride profiles for the 20 year-old parking structure case.

affected by temperature on the basis of the function $H(T)$ (Eq. (28)). Ongoing work on the effect of temperature on water transport will contribute to refine this aspect of the model.

Similar to the case of the hydrated cement pastes presented previously, the heat conductivity was found in [18] using measurements performed on concretes. The heat capacity was measured on concrete samples using the low temperature calorimetry technique (see Fig. 2). A constant value of 1000.0 J/kg/°C/ was used for the simulations.

To simulate the parking slab over 20 years, the boundary conditions must be provided for each variable. The temperature data were provided by the local weather service. The average monthly temperatures measured between 1971 and 2000 were fitted with a sine function. The average temperature is 4 °C with a 16 °C amplitude: $T_\infty = 4 + 16 \sin(2\pi t/365)$ with t expressed in days. The temperature was imposed on both sides of the slab as a convection flux boundary condition: $q_n = h_T(T - T_\infty)$, with $h_T = 10$ m/s.

Relative humidity data on the other hand show less important variations over 1 year. A constant value of 60% in the environment was used, except on the top of the slab when NaCl is applied. In that case, it was assumed that the top surface is exposed to a solution at 100% RH, which corresponds to the water content being equal to the porosity. The relative humidity was converted into water content at the boundaries using the desorption isotherm method proposed by Xi et al. [37]. This corresponding water content w_∞ was then imposed as a convection flux boundary condition: $q_n = h_w(w - w_\infty)$, with $h_w = 3 \times 10^{-8}$ m/s. Values for h_w are proposed in [38].

Applying the boundary conditions for the ionic species poses real difficulties. Sodium chloride is obviously applied only during the winter. But the rate of application strongly depends on the weather conditions and can vary from day to day. To get a better idea of these boundary conditions, solution on the top of the slab was collected at different locations in the parking over the winter in 2004–2005. The locations were predetermined and the brine was collected approximately once per week whenever possible. In some cases, the surface was completely dry, thus yielding nil NaCl concentration for that time and location. In some other cases, there was snow covering the concrete. In that case, snow was collected and melted to analyze the chloride content. The results for two of those locations, showed in Fig. 11a, emphasize the scattered nature of the boundary conditions. To model this, it was assumed that NaCl was applied on top of the slab over a 90-day period following a half-sine function during the coldest part of the year, as shown in Fig. 11b. The sodium chloride concentration reaches a maximum value of 1800 mmol/L. During the application of NaCl, all the other ionic species concentrations on the top boundary were set to zero. This one-year boundary condition cycle, including the 100% RH on top of the slab when NaCl is applied, is repeated over 20 years.

The ingress of chloride in the concrete slab was simulated using the material parameters and boundary conditions described in the previous paragraphs. The calculations were made with a uniform 100-element mesh and with 43,200 s (½ day) time steps. The numerical result, compared to the experimental profile, is shown in Fig. 12. Overall, the model correctly predicts the rate of chloride ingress in the material. Near the surface, the experimental profile exhibits a drop in chloride content that is not predicted by the model. That type of chloride profile near the surface is not uncommon. It has often been attributed to the leaching of chloride ions due to application of water (rain, washing operations, …) on the top surface of a slab. To reproduce this, simulations were performed assuming that water had been applied on the top surface for 30 days before or after exposure to chloride. The results are

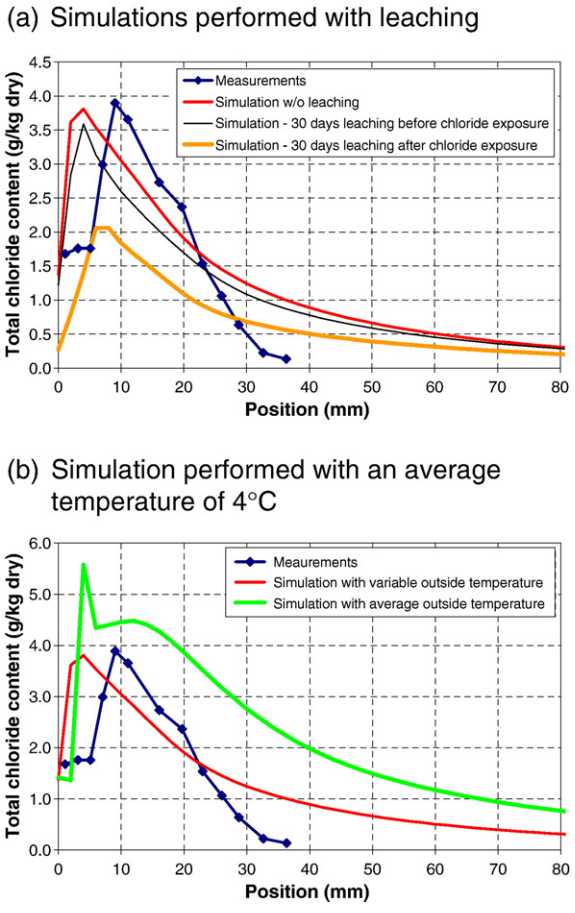

Fig. 13. Effect of leaching and constant temperature on chloride ingress simulation.

shown in Fig. 13a. The model predicts a drop of chloride content near the surface. This drop is more important when water is applied immediately after chloride ingress. However, the numerical results do not match with the localized effect observed from the measurements. From these results, it seems unlikely that the observed chloride drop origins from occasional water application on the concrete. Recent research [39] suggests that this could instead be caused by carbonation, Friedel's salt being unstable when exposed to carbon dioxide.

The simulations showed that the temperature gradients inside the slab are very weak. The heat conduction in the material is fast, which causes the slab to be in near-equilibrium with the outside environment. This suggested that it would be possible to simulate chloride ingress using an average annual temperature instead of the sine function showed in Fig. 11b. The result of this simulation is shown in Fig. 13b. Using an annual average temperature throughout the simulation overestimates chloride ingress. The difference between both cases is caused by the nonlinear effects of temperature on transport and chemistry.

7. Conclusion

The effect of temperature on ionic transport was considered in this paper from three different angles. First, the temperature field is calculated using the basic heat conduction equation. The thermal properties of each phase (hydrated paste, porous solution, aggregates) are lumped into average parameters. An analysis based on the analytical solution to Stefan problem showed that the nonlinearity due to ice formation can be neglected for ionic transport purposes.

The paper then addresses the effect of temperature on ionic diffusion coefficients. Results reveal that it affects the diffusion process similarly for different types of materials. A general function was proposed to estimate variations in diffusion coefficient values when the temperature of the material fluctuates.

Finally, the effect of temperature on chemical reactions was implemented in the model. Under the local equilibrium assumption, it was assumed that temperature affects reactions by modifying the solubility constant. It was taken into account using the Van't Hoff relationship.

Each of the previous topics was implemented in a multiionic transport model. Simulations showed that the model can reproduce chloride profiles for both laboratory experiment and real-life structure. The simulations emphasized that due to the nonlinear nature of the temperature effects, considering an average constant temperature can lead to wrong estimations. The temperature variations have to be considered to evaluate the kinetics of contaminant ingress in structures.

Acknowledgements

The authors would like to acknowledge the participation of the following persons. Yannick Protière provided all the low temperature calorimetry data. Tiewei Zhang was in charge of all the migration experiments presented in the paper. Finally, Joëlle Perreault collected the solution samples in the parking structure during the years 2004 and 2005.

References

[1] E. Samson, J. Marchand, K.A. Snyder, J.J. Beaudoin, Modeling ion and fluid transport in unsaturated cement systems in isothermal conditions, Cement and Concrete Research 35 (2005) 141–153.
[2] Samson E., Marchand J., Modeling the transport of ions in unsaturated cement-based materials, Computers and Structures, submitted for publication.
[3] K.T.B. MacQuarrie, K.U. Mayer, Reactive transport modeling in fractured rock: a state-of-the-science review, Earth-Science Reviews 72 (2005) 189–227.
[4] E. Samson, G. Lemaire, J. Marchand, J.J. Beaudoin, Modeling chemical activity effects in strong ionic solutions, Computational Materials Science 15 (3) (1999) 285–294.
[5] R.J. Millington, J.P. Quirk, Permeability of porous solids, Transactions of the Faraday Society (1961) 1200–1207.
[6] T. Xu, E. Sonnenthal, N. Spycher, K. Pruess, TOUGHREACT—a simulation program for non-isothermal multiphase reactive geochemical transport in variably saturated geologic media: applications to geothermal injectivity and CO_2 geological sequestration, Computers & Geosciences 32 (2006) 145–165.
[7] T. Xu, J. Samper, C. Ayora, M. Manzano, E. Custodio, Modeling of non-isothermal multi-component reactive transport in field scale porous media flow systems, Journal of Hydrology 214 (1999) 144–164.
[8] E. Samson, J. Marchand, Multiionic approaches to model chloride binding in cementitious materials, in: J. Marchand, et al., (Eds.), 2nd Int. Symp. on Advances in Concrete through Science and Engineering, RILEM Proceedings PRO, vol. 51, RILEM Publications, Quebec City, Canada, 2006.
[9] C.A.J. Appelo, Multicomponent ion exchange and chromatography in natural systems, in: Lichtner, et al., (Eds.), Reviews in Mineralogy vol. 34 – Reactive Transport in Porous Media, Mineralogical Society of America, 1996, pp. 193–227.
[10] U.R. Berner, Evolution of pore water chemistry during degradation of cement in a radioactive waste repository environment, Waste Management 12 (1992) 201–219.
[11] B.A. Schrefler, Multiphase flow in deforming porous material, International Journal for Numerical Methods in Engineering 60 (2004) 27–50.
[12] T. Xu, K. Pruess, Modeling multiphase non-isothermal fluid flow and reactive geo-chemical transport in variably saturated fractured rocks: 1. Methodology, American Journal of Science 301 (January 2001) 16–33.
[13] P.C. Lichtner, Continuum formulation of multicomponent–multiphase reactive transport, in: Lichtner, et al., (Eds.), Reviews in Mineralogy vol. 34—Reactive Transport in Porous Media, Mineralogical Society of America, 1996, pp. 1–81.
[14] P. Baggio, C. Bonacina, B. Schrefler, Some considerations on modeling heat and mass transfer in porous media, Transport in Porous Media 28 (1997) 233–251.
[15] D. Gawin, C.E. Majorana, B.A. Schrefler, Numerical analysis of hygro-thermal behaviour and damage of concrete at high temperature, Mechanics of Cohesive-Frictional Materials 4 (1999) 37–74.
[16] A. Saetta, R. Scotta, R. Vitaliani, Analysis of chloride diffusion into partially saturated concrete, ACI Materials Journal 90 (5) (1993) 441–451.
[17] B. Martín-Pérez, S.J. Pantazopoulou, M.D.A. Thomas, Numerical solution of mass transport equations in concrete structures, Computers and Structures 79 (2001) 1251–1264.
[18] K.H. Kim, S.E. Jeon, J.K. Kim, S. Yang, An experimental study on thermal conductivity of concrete, Cement and Concrete Research 33 (2003) 363–371.
[19] J.O'M. Bockris, A.K.N. Reddy, Modern Electrochemistry—An Introduction to an Interdisciplinary Area, Plenum Press, USA, 1970.
[20] J. Bear, Y. Bachmat, Introduction to Modeling of Transport Phenomena in Porous Media, Kluwer Academic Publishers (Pays-Bas), 1991.
[21] N. Özişik, Heat Conduction, 2nd ed. John Wiley, USA, 1993.
[22] Q.T. Pham, The use of lumped capacitance in the finite-element solution of heat conduction problems with phase change, International Journal of Heat and Mass Transfer 29 (1986) 285–291.
[23] M. Daoud, N. Galanis, G. Ballivy, Calculation of the periodic temperature field in a concrete dam, Canadian Journal of Civil Engineering 24 (1997) 772–784.

[24] E. Samson, J. Marchand, K.A. Snyder, Calculation of ionic diffusion coefficients on the basis of migration test results, Materials and Structures 36 (2003) 156–165.
[25] T. Zhang, E. Samson, J. Marchand, Effect of Temperature on Ionic Transport Properties of Concrete, Proceedings of the ConMAT Conference, Published by the University of British Columbia, Vancouver, Canada, August 2005.
[26] American Institute of Physics Handbook, 3rd ed. McGraw Hill, New York, 1972.
[27] Gingras A., Effect of temperature on diffusion in concrete, M.Sc. Thesis (in French), Laval University (Canada), 2005.
[28] J.J. Thomas, D. Rothstein, H.M. Jennings, B.J. Christensen, Effect of hydration temperature on the solubility behavior of Ca-, S-, Al-, and Si-bearing solid phases in Portland cement pastes, Cement and Concrete Research 33 (2003) 2037–2047.
[29] N.F. Ghogomu, R. Therrien, Reactive mass transport modelling in discretely-fractures porous media, computational methods in water resources XIII, in: Bentley, et al., (Eds.), Balkema, Rotterdam, 2000, pp. 285–292.
[30] J.P. Gwo, E.F. D'Azevedo, H. Frenzel, M. Mayes, G.T. Yeh, HBG123D: a high-performance computer model of coupled hydrogeological and biogeochemical processes, Computers & Geosciences 27 (2001) 1231–1242.
[31] J.W. Ball, D.K. Nordstrom, WATEQ4F—User's Manual with Revised Thermodynamic Data Base and Test Cases for Calculating Speciation of Major, Trace and Redox Elements in Natural Waters: U.S. Geological Survey Open-File Report, 1991, pp. 90–129.
[32] Y. Maltais, E. Samson, J. Marchand, Predicting the durability of Portland cement systems in aggresive environments—laboratory validation, Cement and Concrete Research 34 (2004) 1579–1589.
[33] G. Akerlof, G. Kegeles, Thermodynamics of sodium hydroxide solutions, Journal of the American Chemical Society 62 (1940) 620–640.
[34] R.A. Robinson, R.H. Stokes, Electrolyte Solutions, 2nd ed.Butterworths, London, 1959.
[35] Planel D., Les effets couplés de la précipitation d'espèces secondaires sur le comportement mécanique et la dégradation chimique des bétons, Ph.D. Thesis, Université de Marne-la-Vallé (France), 2002 (in French).
[36] C. Hall, Water sorptivity of mortars and concretes: a review, Magazine of Concrete Research 41 (147) (1989) 51–61.
[37] Y. Xi, Z.P. Bažant, H.M. Jenning, Moisture diffusion in cementitious materials—adsorption isotherms, Advanced Cement Based Materials 1 (1994) 248–257.
[38] K. Sakata, A study on moisture diffusion in drying and drying shrinkage of concrete, Cement and Concrete Research 13 (1983) 216–224.
[39] T. Ishida, K. Kawai, R. Sato, Experimental study on decomposition processes of Friedel's salt due to carbonation, in: K. Kovler (Ed.), Int. RILEM-JCI Seminar on Concrete Durability (ConcreteLife'06), RILEM Proceedings, vol. 46, RILEM Publications, Ein-Bokek, 2006, pp. 51–58 (Israel).